

# Photonuclear Production of $^{195m}\text{Pt}$ for Medical Applications: Cross Sections and Energy Thresholds

J. Song,<sup>1,2,\*</sup> J. Nolen,<sup>1</sup> D. Rotsch,<sup>1,3</sup> R. Gampa,<sup>1</sup> R. M. de Kruijff,<sup>1</sup> T. Brossard,<sup>4</sup> C. R. Howell,<sup>5,6</sup>  
F. Krishichayan,<sup>5,6</sup> S. W. Finch,<sup>5,6</sup> Y. K. Wu,<sup>5,6</sup> S. Mikhailov,<sup>6</sup> M. W. Ahmed,<sup>6,7</sup> and R. V. F. Janssens<sup>6,8</sup>

<sup>1</sup>*Physics Division, Argonne National Laboratory, Lemont, IL 60439 USA*

<sup>2</sup>*Facility for Rare Isotope Beams, Michigan State University, East Lansing, MI 48824 USA*

<sup>3</sup>*Radioisotope Science and Technology Division, Oak Ridge National Laboratory, Oak Ridge, TN 37830, USA*

<sup>4</sup>*Chemical & Fuel Cycle Technologies Division, Argonne National Laboratory, Lemont, IL 60439 USA*

<sup>5</sup>*Department of Physics, Duke University, Durham, NC 27708-0308, USA*

<sup>6</sup>*Triangle Universities Nuclear Laboratory, Durham, NC 27708-0308, USA*

<sup>7</sup>*Department of Mathematics and Physics, North Carolina Central University, Durham, NC 27707, USA*

<sup>8</sup>*Department of Physics & Astronomy, University of North Carolina at Chapel Hill, Chapel Hill, NC 27599-3255, USA*

(Dated: February 10, 2026)

Platinum radioisotopes are of growing interest for targeted cancer therapy and diagnostic imaging because their decay delivers highly localized radiation doses in tissue, herewith enabling precise DNA damage through Auger-electron emission. Developing production technologies that provide platinum isotopes with high specific activity is therefore essential, and photonuclear reactions on stable nuclei offer a viable accelerator-based route when supported by reliable cross-section data. We report photonuclear cross-section measurements for the  $^{197}\text{Au}(\gamma,\text{pn})^{195m}\text{Pt}$  reaction at incident  $\gamma$ -ray energies of 27, 29, and 31 MeV using the activation method. The measurements were performed by irradiating a stack of concentric-ring gold targets with a quasi-monoenergetic  $\gamma$ -ray beam provided by the High Intensity Gamma-ray Source (HI $\gamma$ S). The induced  $^{195m}\text{Pt}$  activity was quantified using off-line  $\gamma$ -ray spectroscopy. The present results provide the first experimental information in the energy region where the  $^{197}\text{Au}(\gamma,\text{pn})^{195m}\text{Pt}$  reaction becomes significant and demonstrate the minimum energy requirements and feasibility of producing  $^{195m}\text{Pt}$  via photonuclear reactions using electron accelerator facilities. These measurements indicate that electron energies of  $\geq 50$  MeV are required to achieve practically meaningful production yields.

## I. INTRODUCTION

Platinum-195m ( $^{195m}\text{Pt}$ ) is a metastable radionuclide with a half-life of about 4 days that decays via isomeric transitions. Because of its highly internally converted decay,  $^{195m}\text{Pt}$  emits a large number of low-energy Auger electrons, which deposit their energy over nanometer-scale distances and have attracted interest for targeted Auger-electron therapy and theranostic applications [1, 2]. In addition, the emission of a 98.9-keV  $\gamma$ -ray makes  $^{195m}\text{Pt}$  suitable for quantitative SPECT imaging [3]. The medical relevance of  $^{195m}\text{Pt}$  is closely linked to platinum-based chemotherapy. Platinum compounds, such as cisplatin, are widely used anticancer drugs, and radiolabeling these agents with  $^{195m}\text{Pt}$  enables direct imaging of their biodistribution and pharmacokinetics without altering their chemical structure. Preclinical studies have demonstrated the feasibility of SPECT imaging and quantitative analysis using  $^{195m}\text{Pt}$ -labeled compounds [3, 4], and more recent translational work has further highlighted the potential of  $^{195m}\text{Pt}$  for imaging chemotherapy delivery *in vivo* [5].

Production of  $^{195m}\text{Pt}$  has traditionally relied on reactor-based routes involving neutron capture on enriched iridium targets [6]. Although these methods can provide substantial yields, they may be limited in achievable specific activity due to the presence of stable

platinum isotopes. Accelerator-based production using charged particles, such as the  $^{192}\text{Os}(\alpha,\text{n})^{195m}\text{Pt}$  reaction, has been shown to improve specific activity, but typically requires enriched targets and is constrained by available beam currents [7]. Production of  $^{195m}\text{Pt}$  via photonuclear reactions using electron accelerators has received comparatively little experimental attention [8]. This approach is attractive because photonuclear reactions can produce the desired radionuclide in a chemically distinct target material, herewith enabling efficient chemical separation and potentially high specific activity, an important requirement for Auger-electron-emitting radionuclides [2]. For feasibility studies of photonuclear production of  $^{195m}\text{Pt}$ , reliable cross-section data for the relevant reactions are required. For  $^{195m}\text{Pt}$ -based radiopharmaceuticals, the effective specific activity is governed, not only by the total platinum content, but also by the isomer-to-ground-state production ratio. Theoretical predictions based on TALYS [9] indicate that this ratio remains  $\approx 1$  for photon energies above 30 MeV.

The present work focuses on the production of  $^{195m}\text{Pt}$  via the  $^{197}\text{Au}(\gamma,\text{pn})^{195m}\text{Pt}$  reaction. The metastable isomer emits a characteristic 98.9-keV  $\gamma$ -ray with a half-life of 4.01 days, allowing selective identification of the reaction channel using off-line  $\gamma$ -ray spectroscopy. Photonuclear reaction rates were determined using an activation method, as described in Sec. II and III. The measured cross sections are presented in Sec. IV and the feasibility of producing  $^{195m}\text{Pt}$  via photonuclear reactions is discussed in Sec. V.

\* [songj@frib.msu.edu](mailto:songj@frib.msu.edu)

## II. METHOD

When a photon beam irradiates  $^{197}\text{Au}$ , radioactive nuclides are produced via photonuclear reactions, including  $^{197}\text{Au}(\gamma, \text{pn})^{195m}\text{Pt}$  and  $^{197}\text{Au}(\gamma, 2n)^{195}\text{Au}$ , which both decay with a branch emitting the 98.9-keV  $\gamma$ -ray. The observed counts of this 98.9-keV peak contain contributions from the decays of both  $^{195m}\text{Pt}$  and  $^{195}\text{Au}$ . The simplified decay schemes for  $^{195m}\text{Pt}$  and  $^{195}\text{Au}$  are presented in Fig. 1. The relationship between the observed  $\gamma$ -ray counts and the number of radioactive nuclei can be written as

$$c_{\text{all}} \cdot N_0 = n_0 e^{-\lambda t_c} (1 - e^{-\lambda t_m}), \quad (1)$$

where  $N_0$  denotes the observed  $\gamma$ -ray counts and  $n_0$  is the number of radioactive nuclei at the end of bombardment (EOB). Here,  $c_{\text{all}}$  is the overall correction factor, which accounts for detector efficiency, detector dead time,  $\gamma$  branching ratio,  $\gamma$ -ray attenuation in the target, and self-absorption effects. The symbols  $\lambda$ ,  $t_c$ , and  $t_m$  denote the decay constant, cooling time, and measurement time, respectively. Because the observed  $\gamma$ -ray counts represent a superposition of contributions from the two nuclides, measurements performed at different cooling times allow the individual contributions from  $^{195}\text{Au}$  and  $^{195m}\text{Pt}$  to be separated.

In this work, three measurements were performed using different cooling times: a few hours after the end of the bombardment (EOB),  $\approx 1$  week, and  $\approx 2$  weeks later. The corrected  $\gamma$ -ray counts for  $i$ -th measurement can be expressed as

$$N_i = \sum_k N_{ik} = \sum_k n_{0k} e^{-\lambda_k t_{c,i}} (1 - e^{-\lambda_k t_{m,i}}) \quad (2)$$

where  $k$  labels the nuclides ( $k=1$  for  $^{195}\text{Au}$  and  $k=2$  for  $^{195m}\text{Pt}$ );  $N_i$  represents the corrected number of decay events corresponding to the observed  $\gamma$ -ray counts after applying the overall correction factor  $c_{\text{all}}$ . The  $t_{c,i}$  and  $t_{m,i}$  symbols are the cooling time and measurement time for the  $i$ -th measurement, respectively. For convenience, the above expression can be rewritten in linear form as

$$N_i = \alpha_i n_{01} + \beta_i n_{02} \quad (3)$$

with

$$\alpha_i = e^{-\lambda_1 t_{c,i}} (1 - e^{-\lambda_1 t_{m,i}}), \beta_i = e^{-\lambda_2 t_{c,i}} (1 - e^{-\lambda_2 t_{m,i}})$$

The parameters  $n_{01}$  and  $n_{02}$  were determined by a weighted least-squares fit (see Appendix A for details). The solution can be written explicitly as

$$\begin{pmatrix} n_{01} \\ n_{02} \end{pmatrix} = \frac{1}{D} \begin{pmatrix} \sum \frac{\beta_i^2}{\Delta N_i^2} & -\sum \frac{\alpha_i \beta_i}{\Delta N_i^2} \\ -\sum \frac{\beta_i \alpha_i}{\Delta N_i^2} & \sum \frac{\alpha_i^2}{\Delta N_i^2} \end{pmatrix} \begin{pmatrix} \sum \frac{\alpha_i}{\Delta N_i^2} N_i \\ \sum \frac{\beta_i}{\Delta N_i^2} N_i \end{pmatrix} \quad (4)$$

Statistical uncertainties of  $n_{01}$  and  $n_{02}$  are given by

$$\Delta n_{01} = \sqrt{\frac{1}{D} \sum_{i=1}^3 \frac{\beta_i^2}{\Delta N_i^2}}, \Delta n_{02} = \sqrt{\frac{1}{D} \sum_{i=1}^3 \frac{\alpha_i^2}{\Delta N_i^2}} \quad (5)$$

Using Eqs. 4 and 5, the  $n_{01}$  and  $n_{02}$  parameters, including associated statistical uncertainties, can be extracted from the observed  $\gamma$ -ray counts,  $N_i$ .

## III. EXPERIMENT

A stack of five targets, each divided into three segments [11], was irradiated at seven different central photon beam energies at the High Intensity Gamma-ray Source (HI $\gamma$ S) [12]. Owing to the radial energy gradient across the target stack, the photon energy at the outermost ring was typically close to the central energy of the subsequent lower-energy irradiation, providing an internal consistency check for the measurements (see ref. [11] for details). Using targets composed of three concentric segments, cross sections for the  $^{197}\text{Au}(\gamma, \text{pn})^{195m}\text{Pt}$  reaction were obtained at a total of 3 distinct photon energies for the 31 MeV run, as the cross sections are extremely low below 30 MeV. Each irradiation was performed for 8–12 hours using a photon beam with fluxes in the range of  $10^8$ – $10^9$   $\gamma/s$ . Detailed information on incident beam flux, irradiation time, target thickness, and beam energy and flux at each segment is summarized in Tables III, IV, and VIII of Ref. [11]. The measurement and cooling times for 31 MeV run are summarized in Table I.

TABLE I. Summary of counting periods. The measurement time ( $t_m$ ) and cooling time ( $t_c$ ) are given in hours for each segment.

$E_\gamma$ (MeV)	seg. 1		seg. 2		seg. 3	
	31.05		29.25		27.24	
run	$t_m$	$t_c$	$t_m$	$t_c$	$t_m$	$t_c$
1	5	-	5	-	10	-
2	7	146.29	13	151.58	12	188.19
3	24	310.59	18	332.03	24	353.69

The  $\gamma$ -ray spectra measured for segment 1, the innermost segment, at three different times are presented in Fig. 2 following irradiation: a few hours after the end of bombardment (EOB), one week, and two weeks later. The data accumulation times for the three measurements were 5, 7, and 24 h, respectively. The full spectrum measured at the earliest time (see Fig. 2 (a)) exhibits multiple  $\gamma$ -ray lines originating from activation products such as  $^{196g,196m1,196m2}\text{Au}$  and  $^{194}\text{Au}$  in the gold target. Among these, the  $\gamma$ -ray line at 98.9 keV is of particular interest, as it is emitted by both  $^{195m}\text{Pt}$  and  $^{195}\text{Au}$ , whose individual contributions cannot be distinguished using only this single measurement. The expanded spectra around the 98.9-keV region (see Figs. 2 (b)–(d)) demonstrate a clear evolution of the relative peak intensities with cooling time. At early times after irradiation, the spectrum is dominated by contributions from shorter-lived nuclides, whereas measurements performed after longer cooling times increasingly emphasize the decay of

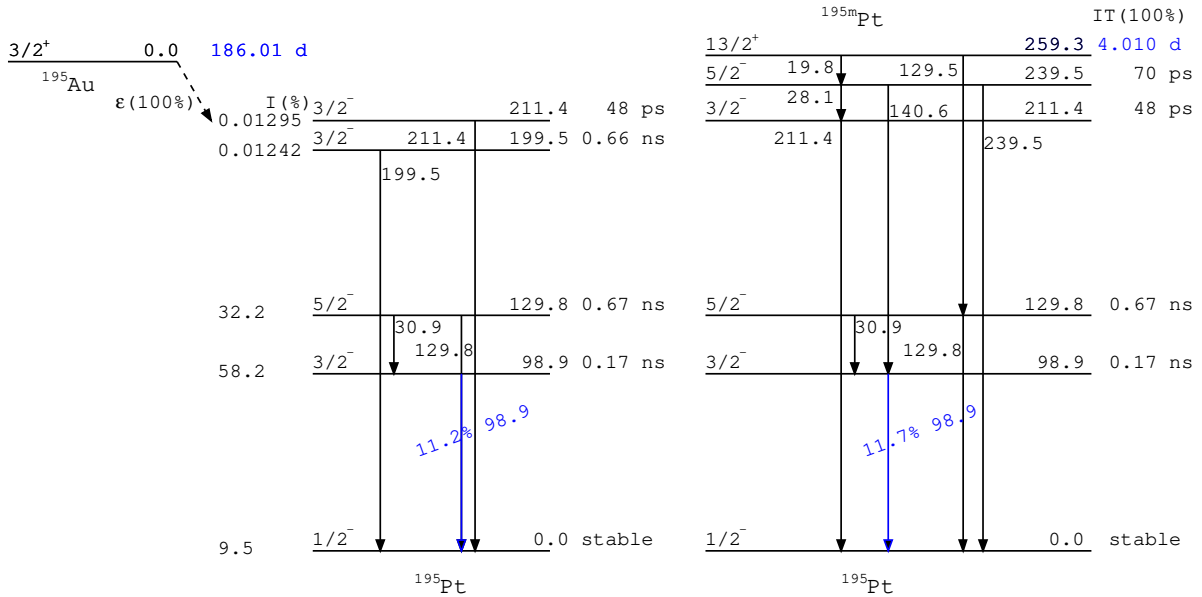


FIG. 1. Simplified decay schemes for the  $^{195}\text{Au}$  and  $^{195m}\text{Pt}$  nuclei. The selected  $\gamma$ -ray lines (blue) were used in the analysis. The decay  $\gamma$  energies and relative intensities are adopted from the National Nuclear Data Center (NNDC) [10].

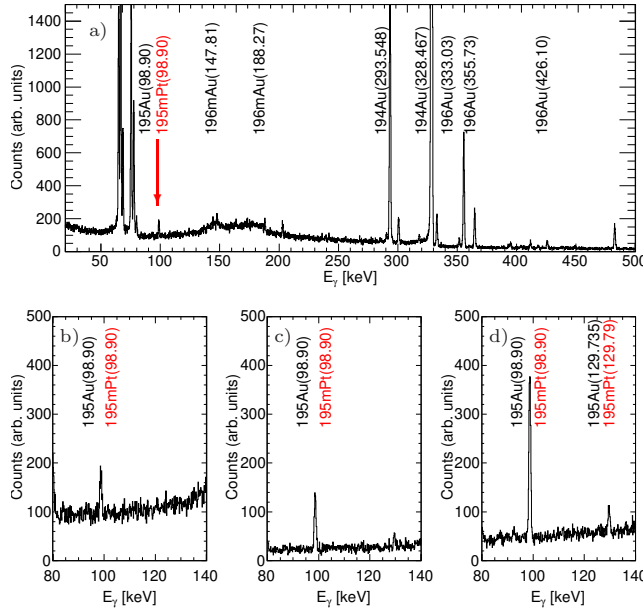


FIG. 2. Full  $\gamma$ -ray spectrum for target segment 1 measured a few hours after the end of bombardment (EOB) (a), and expanded  $\gamma$ -ray spectra around the 98.9-keV peak measured a few hours after EOB (b), one week (c) and two weeks later (d). The 98.9 keV  $\gamma$ -ray line emitted by both  $^{195m}\text{Pt}$  and  $^{195}\text{Au}$  is indicated. The accumulated measurement times for the three measurements were 5, 7, and 24 h, respectively.

longer-lived reaction products. This temporal variation arises from the different half-lives of  $^{195m}\text{Pt}$  ( $T_{1/2} = 4.01$  d) and  $^{195}\text{Au}$  ( $T_{1/2} = 186.01$  d), and enables their in-

dividual activities to be disentangled through measurements performed at multiple cooling times. The systematic change in the 98.9-keV peak intensity as a function of cooling time provides the experimental basis of the approach for the activity decomposition described in Sec. II. By combining the spectra measured at different cooling times with a least-squares analysis, the initial activities of the contributing nuclides can be extracted reliably, despite the spectral overlap at this 98.9-keV  $\gamma$ -ray energy.

#### IV. RESULTS

The photonuclear cross sections corresponding to the number of radioactive nuclei at EOB,  $n_{01}$  and  $n_{02}$  can be expressed as

$$\sigma_i = \frac{\lambda_i n_{0i}}{N_T I_0 (1 - e^{-\lambda_i t_0})} \quad (6)$$

Here  $N_T$ ,  $I_0$  and  $t_0$  represent the number of target nuclei, incident photon flux, and irradiation time, respectively. The statistical uncertainty is evaluated using Eq. 5. Three sources of systematic uncertainty arising from the  $\gamma$ -ray branching ratio, detector efficiency and beam flux are considered. The total systematic uncertainty can therefore be expressed as

$$\frac{\Delta\sigma}{\sigma} = \sqrt{\left(\frac{\Delta I_0}{I_0}\right)^2 + \left(\frac{\Delta\epsilon}{\epsilon}\right)^2 + \left(\frac{\Delta I_{br}}{I_{br}}\right)^2} \quad (7)$$

where  $\Delta I_0$ ,  $\Delta\epsilon$ , and  $\Delta I_{br}$  denote the uncertainties associated with photon beam flux, HPGe detector efficiency, and the  $\gamma$  branching ratio, respectively. The uncertainties in the photon beam flux and HPGe detector efficiency

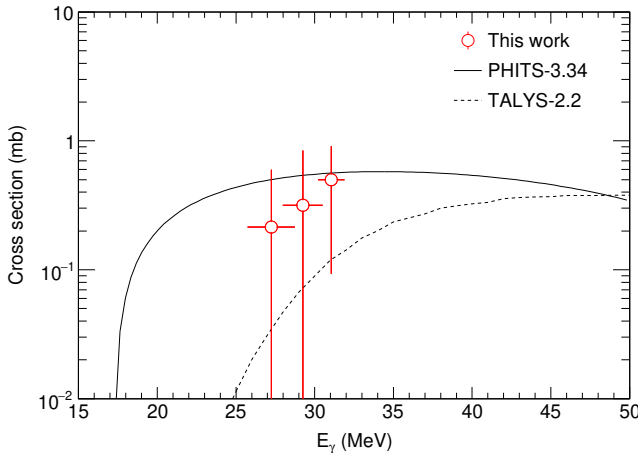


FIG. 3. Excitation function of the  $^{197}\text{Au}(\gamma, \text{pn})^{195m}\text{Pt}$  reaction as a function of incident  $\gamma$ -ray energy. Red symbols represent the cross sections measured in this work. Vertical error bars indicate the total experiment uncertainties defined in Eq. 7, while horizontal error bars indicate the energy spread of the incident  $\gamma$ -ray beam. The experimental results are compared with theoretical predictions calculated using the PHITS-3.34 (solid black line) [13] and TALYS-2.2 codes (dotted black line) [9].

are  $\approx 5\%$  and  $8\%$ , while uncertainties of the  $\gamma$  branching ratios are given in Table II.

TABLE II. Decay information for the measured  $^{195m}\text{Pt}$  and  $^{195}\text{Au}$  nuclei. Data are taken from the National Nuclear Data Center (NNDC) [10].

Nucl.	decay mode	half-life	$\gamma$ energy	$\gamma$ branching ratio	
			d	keV	%
$^{195m}\text{Pt}$	IT	100 %	4.010 (5)	98.9	11.7 (8)
$^{195}\text{Au}$	$\epsilon$	100 %	186.01 (6)	98.9	11.21 (15)

The excitation function of the  $^{197}\text{Au}(\gamma, \text{pn})^{195m}\text{Pt}$  measured at incident  $\gamma$ -ray energies of 27, 29, and 31 MeV is illustrated in Fig. 3. The measured cross sections exhibit a clear increase with photon energy, reflecting the opening and growing contribution of the  $(\gamma, \text{pn})$  reaction channel above threshold. Vertical error bars represent the total experimental uncertainties, which is the combined statistical (from Eq. 5) and systematic (from Eq. 7) uncertainties. The statistical uncertainty of the observed  $\gamma$ -ray counts is the dominant contribution to the overall uncertainty in extracting cross sections. This is primarily due to the relatively small contribution of the  $^{195m}\text{Pt}$  decay to the mixed 98.9-keV  $\gamma$ -ray peak compared to that of  $^{195}\text{Au}$ , with the  $^{195m}\text{Pt}$  activity accounting for only about 5-18 % of the total activity at EOB. For each segment, the measured  $^{195m}\text{Pt}$  activity at EOB ranges from  $\approx 4 \times 10^{-14}$  to  $1.2 \times 10^{-13}$  Ci. As a result, the counting statistics for  $^{195m}\text{Pt}$  are limited and strong anti-correlation arises between the fitted activities. Con-

ssequently, the relative uncertainty of the extracted  $^{195m}\text{Pt}$  activity is comparable to, or larger than, that of the measured cross section.

The measured cross sections are compared with theoretical predictions calculated using the PHITS [13] and TALYS [9] codes. Our data are consistent with the overall trend of both models within the experimental uncertainties. These results provide the first experimental constraints on the cross section for the  $^{197}\text{Au}(\gamma, \text{pn})^{195m}\text{Pt}$  reaction in the energy region just above reaction threshold.

## V. CONCLUSION

We have measured the photonuclear cross sections for the  $^{197}\text{Au}(\gamma, \text{pn})^{195m}\text{Pt}$  reaction using a quasi-monoenergetic  $\gamma$ -ray beam at incident energies of 27, 29, and 31 MeV at  $\text{HI}\gamma\text{S}$ . The observed 98.9-keV  $\gamma$ -ray peak contains contributions from the decays of both  $^{195}\text{Au}$  and  $^{195m}\text{Pt}$ . These contributions were successfully extracted using a least-squares analysis of measurements performed at multiple cooling times. For the first time, cross sections were experimentally determined in the vicinity of the reaction threshold. No statistically significant 98.9-keV peak attributable to  $^{195m}\text{Pt}$  was observed for irradiation energies below 27 MeV, despite the reaction threshold energy of  $E_{th} = 13.96$  MeV, indicating that, under present experimental conditions, specifically a photon flux of  $\approx 10^8 \gamma/\text{s}$  and irradiation time 8-10 hours, the production yield is insufficient to detect this rare reaction channel at lower energies. The measured cross sections indicate that the  $^{197}\text{Au}(\gamma, \text{pn})^{195m}\text{Pt}$  reaction begins to contribute measurably at incident photon energies of  $\approx 30$  MeV, but remains too weak for practical isotope production with bremsstrahlung  $\gamma$  rays at energies typically available at electron accelerator facilities. Although electron energies around 40 MeV are commonly employed for photonuclear isotope production, the present results suggest that such energies are insufficient to yield meaningful  $^{195m}\text{Pt}$  production under realistic experimental conditions. Combining our results with the model predictions for the excitation function for the  $^{197}\text{Au}(\gamma, \text{pn})^{195m}\text{Pt}$  reaction shown in Fig. 3, we project that efficient production of  $^{195m}\text{Pt}$  via photonuclear reactions in quantities required for applications will require bremsstrahlung photon beams with substantially higher end-point energies than are standard, e.g., on the order of 50-60 MeV. The present results provide experimental constraints on the minimum photon energies relevant for photonuclear production of  $^{195m}\text{Pt}$  and motivate future measurements at higher  $\gamma$ -ray energies, extending beyond 50 MeV at  $\text{HI}\gamma\text{S}$ .

## ACKNOWLEDGMENTS

This research was supported by the U.S. Department of Energy Isotope Program, managed by the Office of Sci-

ence for Isotope R&D and Production, under contract DE-AC02-06CH11357 (Argonne National Laboratory), and the Department of Energy, Office of Nuclear Physics under grant numbers DE-SC0018112, DE-SC0018325, DE-FG02-97ER41033 (TUNL) and DEFG02-97ER41041 (UNC). The authors would like to thank the HI $\gamma$ S operators and staff for their help during the experiments. We gratefully acknowledge the computing resources provided on Bebop, a high-performance computing cluster operated by the Laboratory Computing Resource Center at Argonne National Laboratory.

### Appendix A: Weighted least-squares formalism

From Eq. 2, the measured counts  $N_i$  can be written as

$$N_i = \alpha_i n_{01} + \beta_i n_{02}$$

with

$$\alpha_i = e^{-\lambda_1 t_{c,i}} (1 - e^{-\lambda t_{m,i}}), \beta_i = e^{-\lambda_2 t_{c,i}} (1 - e^{-\lambda t_{m,i}})$$

The parameters  $n_{01}$  and  $n_{02}$  were determined by a weighted least-squares fit. The  $\chi^2$  is defined as

$$\chi^2(n_{01}, n_{02}) = \sum_{i=1}^3 \frac{[N_i - (\alpha_i n_{01} + \beta_i n_{02})]^2}{\Delta N_i^2}$$

where  $\Delta N_i$  denotes the statistical uncertainty of  $N_i$ . The  $\chi^2$  is minimized by solving,

$$\begin{aligned} \frac{\partial}{\partial n_{01}} \chi^2 &= -2 \sum \frac{\alpha_i}{\Delta N_i^2} [N_i - (\alpha_i n_{01} + \beta_i n_{02})] = 0 \\ \frac{\partial}{\partial n_{02}} \chi^2 &= -2 \sum \frac{\beta_i}{\Delta N_i^2} [N_i - (\alpha_i n_{01} + \beta_i n_{02})] = 0 \end{aligned}$$

Minimization of this expression leads a set of normal equations that can be written in matrix form as

$$\begin{pmatrix} \sum \frac{\alpha_i^2}{\Delta N_i^2} & \sum \frac{\alpha_i \beta_i}{\Delta N_i^2} \\ \sum \frac{\beta_i \alpha_i}{\Delta N_i^2} & \sum \frac{\beta_i^2}{\Delta N_i^2} \end{pmatrix} \begin{pmatrix} n_{01} \\ n_{02} \end{pmatrix} = \begin{pmatrix} \sum \frac{\alpha_i}{\Delta N_i^2} N_i \\ \sum \frac{\beta_i}{\Delta N_i^2} N_i \end{pmatrix}$$

The solution can be written explicitly as

$$\begin{pmatrix} n_{01} \\ n_{02} \end{pmatrix} = \frac{1}{D} \begin{pmatrix} \sum \frac{\beta_i^2}{\Delta N_i^2} & -\sum \frac{\alpha_i \beta_i}{\Delta N_i^2} \\ -\sum \frac{\beta_i \alpha_i}{\Delta N_i^2} & \sum \frac{\alpha_i^2}{\Delta N_i^2} \end{pmatrix} \begin{pmatrix} \sum \frac{\alpha_i}{\Delta N_i^2} N_i \\ \sum \frac{\beta_i}{\Delta N_i^2} N_i \end{pmatrix} \quad (A1)$$

$$\text{where } D = \sum \frac{\alpha_i^2}{\Delta N_i^2} \sum \frac{\beta_i^2}{\Delta N_i^2} - \left( \sum \frac{\alpha_i \beta_i}{\Delta N_i^2} \right)^2.$$

The statistical uncertainty is calculated as,

$$\Delta n_{0k}^2 = \sum \left[ \Delta N_i^2 \left( \frac{\partial n_{0k}}{\partial N_i} \right)^2 \right] \quad (A2)$$

To determine the uncertainty in the parameter  $n_{01}$ , we take the partial derivatives of Eq. A2,

$$\frac{\partial n_{01}}{\partial N_j} = \frac{1}{D} \left( \frac{\alpha_j}{\Delta N_j^2} \sum \frac{\beta_i^2}{\Delta N_i^2} - \frac{\beta_j}{\Delta N_j^2} \sum \frac{\alpha_i \beta_i}{\Delta N_i^2} \right)$$

and, from the Eq. A1, the statistical uncertainty of  $n_{01}$  is obtained as

$$\begin{aligned} \Delta n_{01}^2 &= \sum \left[ \Delta N_i^2 \left( \frac{\partial n_{01}}{\partial N_i} \right)^2 \right] \\ &= \frac{1}{D^2} \sum \frac{\beta_i^2}{\Delta N_i^2} \left[ \sum \frac{\alpha_j^2}{\Delta N_j^2} \sum \frac{\beta_i^2}{\Delta N_i^2} - \left( \sum \frac{\alpha_i \beta_i}{\Delta N_i^2} \right)^2 \right] \\ &= \frac{1}{D} \sum \frac{\beta_i^2}{\Delta N_i^2} \end{aligned}$$

Similary, the statistical uncertainty of  $n_{02}$  is obtained as,

$$\begin{aligned} \Delta n_{02}^2 &= \sum \left[ \Delta N_i^2 \left( \frac{\partial n_{02}}{\partial N_i} \right)^2 \right] \\ &= \frac{1}{D^2} \sum \frac{\alpha_i^2}{\Delta N_i^2} \left[ \sum \frac{\alpha_j^2}{\Delta N_j^2} \sum \frac{\beta_i^2}{\Delta N_i^2} - \left( \sum \frac{\alpha_i \beta_i}{\Delta N_i^2} \right)^2 \right] \\ &= \frac{1}{D} \sum \frac{\alpha_i^2}{\Delta N_i^2} \end{aligned}$$

---

[1] R. W. Howell *et al.*, *Radiation Research* **140**, 55 (1994).  
[2] A. Ku *et al.*, *EJNMMI Radiopharmacy and Chemistry* **4**, 27 (2019).  
[3] E. A. Aalbersberg *et al.*, *European Journal of Nuclear Medicine and Molecular Imaging* **44**, 1347 (2017).  
[4] R. H. de Roest *et al.*, *European Journal of Nuclear Medicine and Molecular Imaging* **14** (2024).  
[5] D. S. Hoogenkamp *et al.*, *European Journal of Nuclear Medicine and Molecular Imaging* **15** (2025).  
[6] A. S. Madumarov *et al.*, *Nuclear Medicine and Biology* **134-135**, 108928 (2024).  
[7] K. Hilgers *et al.*, *Applied Radiation and Isotopes* **66**, 545 (2008).  
[8] E. N. Bodnar *et al.*, *Journal of Radioanalytical and Nuclear Chemistry* **305**, 133 (2015).  
[9] A. Koning *et al.*, *Eur. Phys. J. A* **59**, 131 (2023).  
[10] X. Huang and M. Kang, *Nuclear Data Sheets* **121**, 395 (2014).  
[11] J. Song *et al.*, *Phys. Rev. C* **110**, 064604 (2024).  
[12] H. R. Weller *et al.*, *Progress in Particle and Nuclear Physics* **62**, 257 (2009).  
[13] T. Sato *et al.*, *Journal of Nuclear Science and Technology* **61**, 127 (2024).